INSTITUTE OF PHYSICS PUBLISHING PHYSIOLOGICAL MEASUREMENT

Physiol. Meas. **24** (2003) 579–589 PII: S0967-3334(03)59917-8

Static resistivity image of a cubic saline phantom in magnetic resonance electrical impedance tomography (MREIT)

Byung Il Lee[1], Suk Hoon Oh[2], Eung Je Woo[1], Soo Yeol Lee[2], Min Hyoung Cho[2], Ohin Kwon[3], Jin Keun Seo[4] and Woon Sik Baek[1]

[1] College of Electronics and Information, Kyung Hee University, Korea
[2] Graduate School of East–West Medical Sciences, Kyung Hee University, Korea
[3] Department of Mathematics, Konkuk University, Korea
[4] Department of Mathematics, Yonsei University, Korea

E-mail: ejwoo@khu.ac.kr

Received 24 February 2003
Published 30 April 2003
Online at stacks.iop.org/PM/24/579

Abstract

In magnetic resonance electrical impedance tomography (MREIT) we inject currents through electrodes placed on the surface of a subject and try to reconstruct cross-sectional resistivity (or conductivity) images using internal magnetic flux density as well as boundary voltage measurements. In this paper we present a static resistivity image of a cubic saline phantom ($50 \times 50 \times 50$ mm^3) containing a cylindrical sausage object with an average resistivity value of 123.7 Ω cm. Our current MREIT system is based on an experimental 0.3 T MRI scanner and a current injection apparatus. We captured MR phase images of the phantom while injecting currents of 28 mA through two pairs of surface electrodes. We computed current density images from magnetic flux density images that are proportional to the MR phase images. From the current density images and boundary voltage data we reconstructed a cross-sectional resistivity image within a central region of 38.5×38.5 mm^2 at the middle of the phantom using the J-substitution algorithm. The spatial resolution of the reconstructed image was 64×64 and the reconstructed average resistivity of the sausage was 117.7 Ω cm. Even though the error in the reconstructed average resistivity value was small, the relative L^2-error of the reconstructed image was 25.5% due to the noise in measured MR phase images. We expect improvements in the accuracy by utilizing an MRI scanner with higher SNR and increasing the size of voxels scarifying the spatial resolution.

Keywords: MREIT, resistivity image, J-substitution algorithm

1. Introduction

When we inject current I into an electrically conducting body, such as a saline phantom or human subject through a pair of surface electrodes, it creates distributions of voltage V, current density $\mathbf{J}$ and magnetic flux density $\mathbf{B}$. We denote a resistivity distribution of the subject as ρ. Then, we have $\mathbf{J} = -\nabla V/\rho$ and $\mathbf{J} = \nabla \times \mathbf{B}/\mu_0$ where μ_0 is the permeability of the free space and biological tissues. In electrical impedance tomography (EIT), the measured boundary voltage data from surface electrodes are used to reconstruct cross-sectional images of resistivity (or conductivity) distributions. Static imaging in EIT suffers from the ill-posedness of the corresponding inverse problem and most reconstruction algorithms in EIT produce resistivity images with a relatively low spatial resolution and accuracy.

In magnetic resonance electrical impedance tomography (MREIT), we use an MRI scanner to capture images of the induced magnetic flux density $\mathbf{B}$ due to the injection current so that this additional internal information helps us in producing better resistivity images (Zhang 1992, Woo *et al* 1994, Ider and Birgul 1998, Eyuboglu *et al* 2001, Kwon *et al* 2002, Khang *et al* 2002). For the image reconstruction algorithm in MREIT, we can use the J-substitution algorithm developed by Kwon *et al* (2002). Khang *et al* (2002) described the experimental procedure and data processing methods to use the J-substitution algorithm in MREIT. They showed a resistivity image of a saline phantom with an insulating object inside. The image contained a large amount of error in describing the shape of the insulating object. The accuracy of the reconstructed resistivity values was also low due primarily to the low SNR of the 0.3 T experimental MRI scanner used in their study. Their preliminary results showed the feasibility of the method but also the need for more improvements.

When a subject includes an insulating object inside, the current density in the object is zero. This means that the signal (current density) there is zero and any small amount of noise will easily show up. Therefore, in MREIT where we use the internal current density data obtained from the measured magnetic flux density, any subjects including insulating objects are most difficult to image. Fortunately, this kind of resistivity distribution seldom occurs in the human subject. Oh *et al* (2002) showed a better resistivity image using a saline phantom with a cylindrical sausage object inside. The resistivity values of the saline and sausage were within the range of physiologically observed ones. In this paper, we use a similar phantom with a sausage object inside and describe the experimental procedure, noise analysis and improved data processing methods in reconstructing the resistivity image of the saline phantom.

2. Methods

2.1. Phantom experiment

We used our 0.3 T experimental MRI scanner with 25 cm bore shown in figure 1(a). In order to inject current I into a subject, we constructed a constant current source whose output pulse is synchronized with the standard spin–echo pulse sequence shown in figure 1(b). The constant current source was controlled by an 8-bit microcontroller. We used the gate signal synchronized with a 90° RF pulse from the spectrometer (Tecmag Inc., USA) as the trigger signal in the current source. We adjusted amplitudes and durations of injection current pulses using the microcontroller. In order to obtain the image of the internal current density distribution due to the injection current, we used the magnetic resonance current density imaging (MRCDI) technique as described in Scott *et al* (1991, 1992), Eyuboglu *et al* (1998), Gamba and Delpy (1998) and Gamba *et al* (1999).

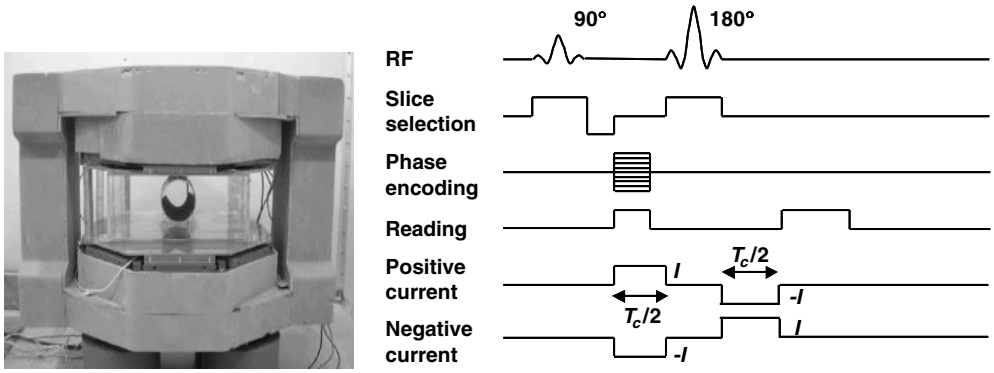

Figure 1. (a) Experimental MRI scanner with 0.3 T permanent main magnet. (b) Spin–echo pulse sequence used in the experiment.

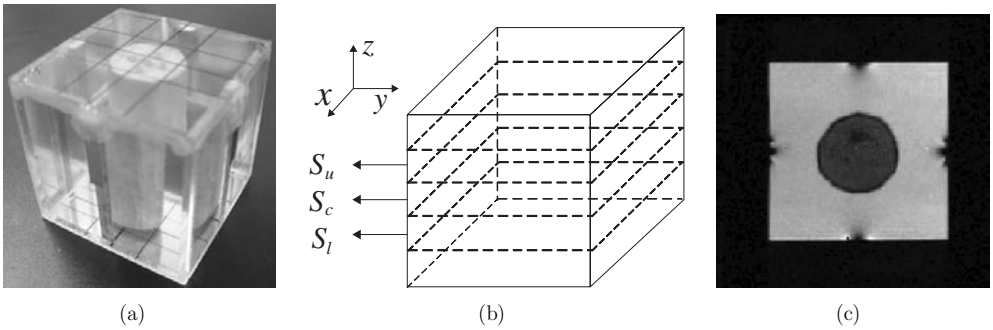

Figure 2. (a) Saline phantom including a cylindrical sausage object, (b) three imaging slices of S_u, S_c and S_l and (c) MR magnitude image at the centre slice S_c.

Since the MRCDI technique used in this paper requires rotations of the subject to measure all three components of the magnetic flux density $\mathbf{B} = (B_x, B_y, B_z)$, we used the cubic phantom ($50 \times 50 \times 50\,\text{mm}^3$, acrylic plastic) shown in figure 2(a). It was filled with a solution containing 12.5 g l^{-1} NaCl and 2 g l^{-1} $CuSO_4 \cdot 5H_2O$. Inside the phantom, a cylindrical sausage object is located around its centre. The diameter and height of the sausage object were 30 and 50 mm, respectively. The resistivity values of the solution and sausage measured by HP4192A Impedance Analyzer (Agilent Technologies Co., USA) at 20–1000 Hz were 50.5 and 123.7 Ω cm, respectively. The standard deviations in the resistivity measurements were 0.49 and 7.3 Ω cm for the solution and sausage, respectively.

We used four copper electrodes ($5 \times 50\,\text{mm}^2$) to inject two different currents. The constant current source selected a pair of electrodes on two opposite sides of the phantom in the vertical direction for the injection current I_1. After collecting all image data for I_1, we switched it to the other electrode pair in the horizontal direction for the injection current I_2. These kinds of two injection currents can provide the uniqueness of the reconstructed resistivity image (Kim *et al* 2002). Injection current pulses of $I = 28$ mA with $T_c/2 = 24$ ms were synchronized with the pulse sequence in figure 1(b). The pulse repetition time was 300 ms and the echo time was 60 ms. The slice thickness was 10 mm and the field of view was 77 mm. In obtaining 128×128 MR images, the number of averagings was 16 and phase encoding step was 128. The voxel size was $0.6 \times 0.6 \times 10\,\text{mm}^3$.

We rotated the phantom twice with the same orientation as described in Khang *et al* (2002) to obtain phase images for B_x, B_y and B_z from three slices of S_u, S_c and S_l shown in figure 2(b). Since we differentiate B_z with respect to x and y in computing the current density $\mathbf{J} = \nabla \times \mathbf{B}/\mu_0$, we acquired one phase image for B_z from the centre slice S_c. We must differentiate B_x and B_y with respect to z as well as y and x, respectively. Therefore, we obtained three phase images from three slices of S_u, S_c and S_l for each of B_x and B_y. Therefore, for each injection current of I_1 and I_2, we acquired seven phase images from the three slices.

Figure 2(c) shows the MR magnitude image of the phantom at the centre slice S_c. The artefacts near the electrodes are due to the susceptibility and RF shielding effect of copper electrodes. The signal-to-noise ratio (SNR) was 27.2 in the solution and 6.86 in the sausage assuming that both solution and sausage are homogeneous.

2.2. Data processing

Khang *et al* (2002) described the details of data processing methods to use the J-substitution algorithm in MREIT including phase unwrapping, geometrical error correction, denoising and curl operation to obtain the current density. In this section, therefore, we only describe the improvements we made in data processing methods.

First, we enhanced the accuracy of the geometrical error correction by imaging a grid phantom in a higher spatial resolution of 256×256 whereas images from the saline phantom were captured with a spatial resolution of 128×128. Second, we employed a better phase unwrapping algorithm. Due to the instability of our 0.3 T MRI scanner in terms of its shielding and temperature controller, we often observe spike-like noise in phase images. Therefore, if we use a simple phase unwrapping algorithm as is done by Khang *et al* (2002), a time-consuming manual correction process is often required. In this paper, we used Goldstein's branch cut algorithm (Ghiglia and Pritt 1998) that does not require any manual process. It is a kind of path-following method and successfully unwraps noisy phase images. After the phase unwrapping, phase images were converted to magnetic flux density images by an appropriate scaling as described in Khang *et al* (2002).

As shown in figure 2(c), the phantom occupies a region of 83×83 pixels in the 128×128 MR image. Since there are artefacts near electrodes, we extracted magnetic flux density images of 66×66 pixels within the region of 83×83 pixels. Before we differentiate images of B_x, B_y and B_z, we applied the total variation-based denoising algorithm by Chan *et al* (2000).

The current density $\mathbf{J} = (J_x, J_y, J_z)$ is computed in the region of 64×64 pixels as follows,

$$J_x = \frac{1}{8\mu_0 \Delta y} B_z^{S_c} \otimes D^T - \frac{1}{2\mu_0 \Delta z} \left(B_y^{S_u} - B_y^{S_l} \right) \tag{1}$$

$$J_y = \frac{1}{2\mu_0 \Delta z} \left(B_x^{S_u} - B_x^{S_l} \right) - \frac{1}{8\mu_0 \Delta x} B_z^{S_c} \otimes D \tag{2}$$

$$J_z = \frac{1}{8\mu_0 \Delta x} B_y^{S_c} \otimes D - \frac{1}{8\mu_0 \Delta y} B_x^{S_c} \otimes D^T \tag{3}$$

where $\otimes$ means the two-dimensional convolution operation, $\mu_0 = 4\pi \times 10^{-7}$ H m^{-1}, B_q^S is the q-component of the magnetic flux density from the slice S,

$$\Delta x = \Delta y = 0.6\,\text{mm}, \qquad \Delta z = 10\,\text{mm}, \qquad D = \begin{bmatrix} -1 & 0 & 1 \\ -2 & 0 & 2 \\ -1 & 0 & 1 \end{bmatrix}$$

and D^T is the transpose of D.

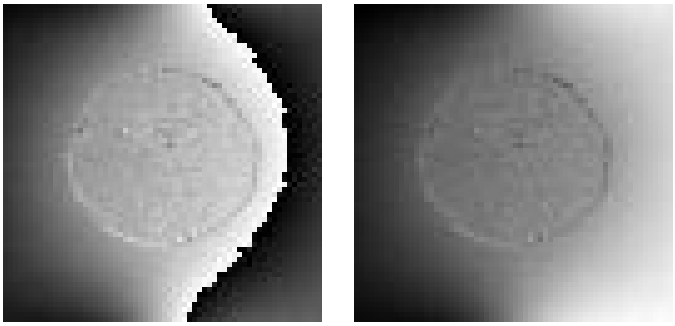

(a) (b)

Figure 3. Phase image for B_z at the centre slice S_c of the phantom for the vertical injection current I_1 (a) before and (b) after unwrapping.

Since the resistivity distribution of the phantom does not change along the z-direction and the length of the electrodes covers the full height of the phantom, J_z is supposed to be zero. Though the computed values of J_z from measured B_x and B_y using (3) were not zero due to the noise, inhomogeneous resistivity values of the sausage and other factors, J_z was much smaller than J_x and J_y. Therefore, we applied the two-dimensional J-substitution algorithm using only J_x and J_y to reconstruct the cross-sectional resistivity image ρ. In solving the forward problem during the resistivity image reconstruction, we used the current density values from (1) and (2) on four edges of the 64×64 image as Neumann boundary conditions.

In applying the J-substitution algorithm, we need to use at least one measured voltage between a pair of electrodes to appropriately scale the reconstructed resistivity image (Kwon *et al* 2002). For each injection current, the measured voltage between two current injection electrodes was bigger than the corresponding voltage predicted by a three-dimensional forward solver (Lee *et al* 2002) since we ended up using the two-electrode measurement method. When we measured the voltage between the other two electrodes where no current flows, the measured voltage was almost zero due to the symmetry of the phantom. Therefore, in this paper, we had to use the voltage data computed from the three-dimensional forward solver instead of the measured data. This may have caused a scaling error in the reconstructed resistivity image. We will discuss this voltage measurement problem later in this paper.

3. Results

Figure 3 shows the wrapped and unwrapped phase image for B_z at the centre slice S_c. Figures 4(a), (b) and (c) are images of B_x, B_y and B_z, respectively, at the same slice of S_c before denoising for the vertical injection current I_1. Figures 4(d), (e) and (f) are the corresponding images after denoising. The noise standard deviation in the magnetic flux density image can be estimated as

$$\sigma_B = \frac{1}{2\gamma T_c \,\mathrm{SNR}} \tag{4}$$

where $\gamma = 26.75 \times 10^7\,\mathrm{rad\,s^{-1}\,T^{-1}}$ and SNR is the SNR of the MR magnitude image (Scott *et al* 1992). With $T_c = 48$ ms, we obtain $\sigma_B = 1.43 \times 10^{-9}$ T in the solution and 5.68×10^{-9} T in the sausage. Figure 5(a) shows horizontal profiles at the centre of two B_z images in figures 4(c) and (f). Figure 5(b) is the difference between these two horizontal profiles. In order to

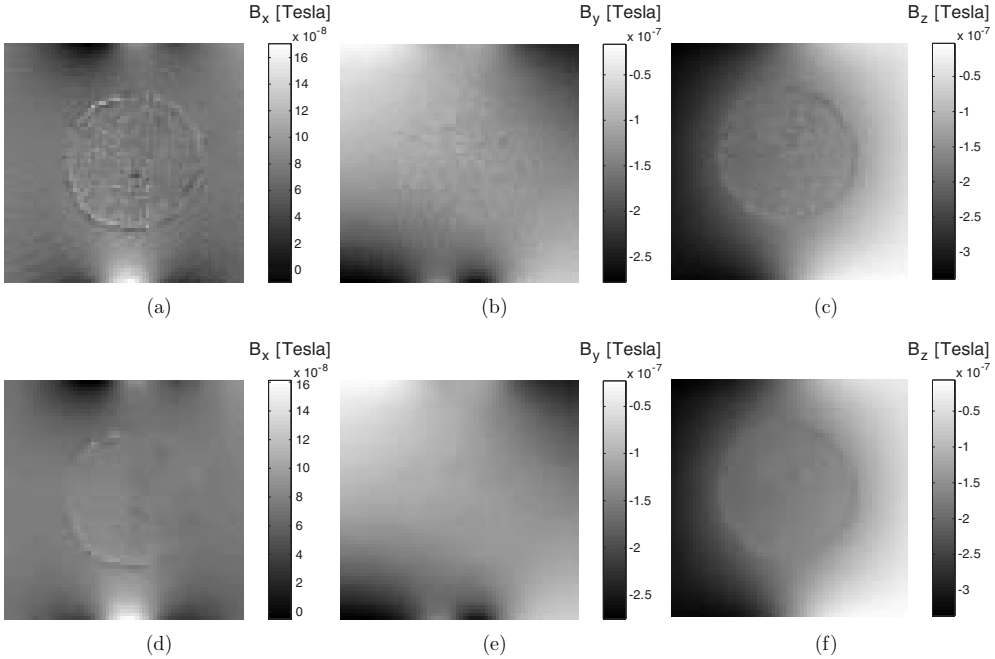

Figure 4. Magnetic flux density images at the centre slice S_c for the vertical injection current I_1: (a) B_x, (b) B_y, (c) B_z, (d) B_x after denoising, (e) B_y after denoising and (f) B_z after denoising.

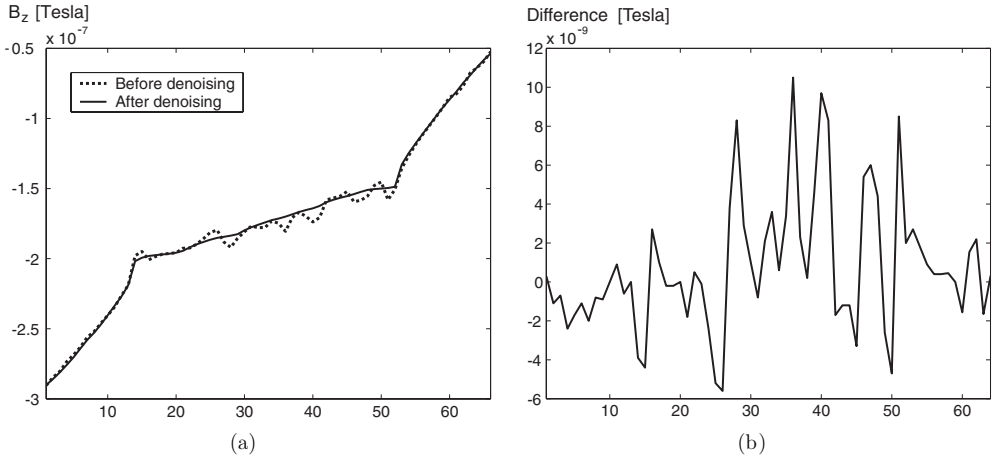

Figure 5. (a) Horizontal profiles at the centre of two B_z images in figures 4(c) and (f). (b) Difference between the two profiles in (a).

estimate the noise standard deviations of the measured magnetic flux density images, we computed the difference between two B_z images in figure 4(f) after denoising and (c) before denoising. The standard deviations in the difference image were 1.89×10^{-9} and 4.59×10^{-9} T in the solution and sausage, respectively. These values are comparable to the estimated values using (4).

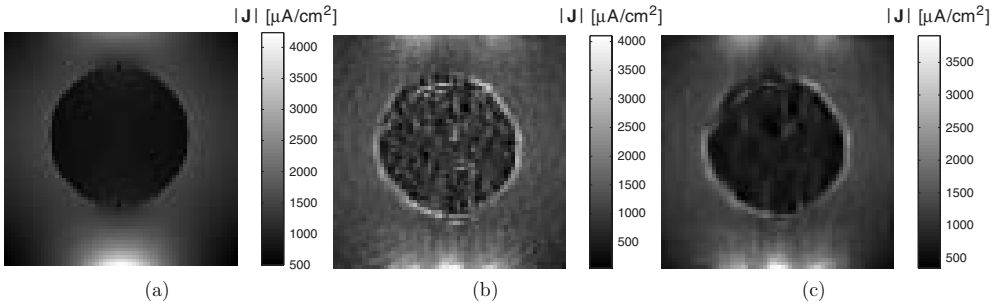

(a) (b) (c)

Figure 6. Images of the magnitude of the current density $|\mathbf{J}|$ for the vertical injection current I_1 from (a) the three-dimensional forward solver, (b) measured magnetic flux densities without denoising and (c) with denoising.

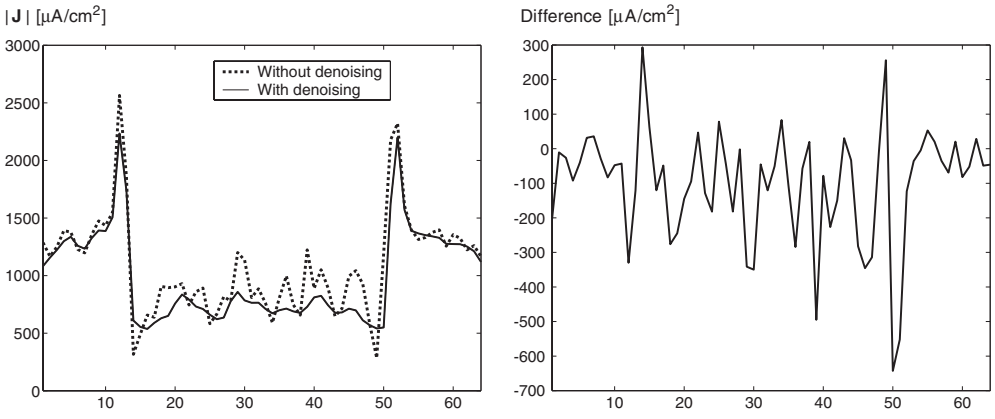

(a) (b)

Figure 7. (a) Horizontal profiles at the centre of two $|\mathbf{J}|$ images in figures 6(b) and (c). (b) Difference between the two profiles in (a).

Figure 6(a) shows the magnitude of the current density $|\mathbf{J}|$ for the vertical injection current I_1 computed from the finite element model of the saline phantom with the true resistivity distribution using the three-dimensional forward solver by Lee *et al* (2002). Figure 6(b) is the corresponding image obtained from the measured magnetic flux densities without denoising. Figure 6(c) is the same image using the measured magnetic flux densities with denoising. The noise standard deviations in J_x and J_y were given by Scott *et al* (1992) as

$$\sigma_{J_x} = \frac{1}{2\mu_0 \gamma T_c \ \mathrm{SNR}} \sqrt{\left(\frac{F_y}{\Delta y}\right)^2 + \left(\frac{F_z}{\Delta z}\right)^2} \tag{5}$$

$$\sigma_{J_y} = \frac{1}{2\mu_0 \gamma T_c \ \mathrm{SNR}} \sqrt{\left(\frac{F_x}{\Delta x}\right)^2 + \left(\frac{F_z}{\Delta z}\right)^2} \tag{6}$$

where $F_x = F_y = \sqrt{3}/4$ and $F_z = 1/\sqrt{2}$ in our case. The computed values are $\sigma_{J_x} = \sigma_{J_y} = 82.6\ \mu\mathrm{A\ cm}^{-2}$ within the solution and $327.6\ \mu\mathrm{A\ cm}^{-2}$ within the sausage. Since $|\mathbf{J}| = \sqrt{J_x^2 + J_y^2}$, the noise standard deviations in the image shown in figure 6(b) are supposed to be about 54 and 215 $\mu\mathrm{A\ cm}^{-2}$ within the solution and sausage, respectively. Figure 7(a) shows horizontal profiles at the centre of two $|\mathbf{J}|$ images in figures 6(b) and (c).

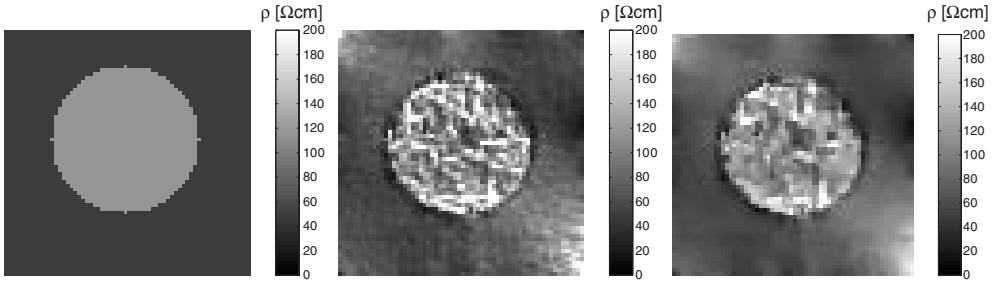

(a) (b) (c)

Figure 8. (a) True resistivity image assuming the sausage is homogeneous, (b) reconstructed resistivity image without denoising and (c) with denoising.

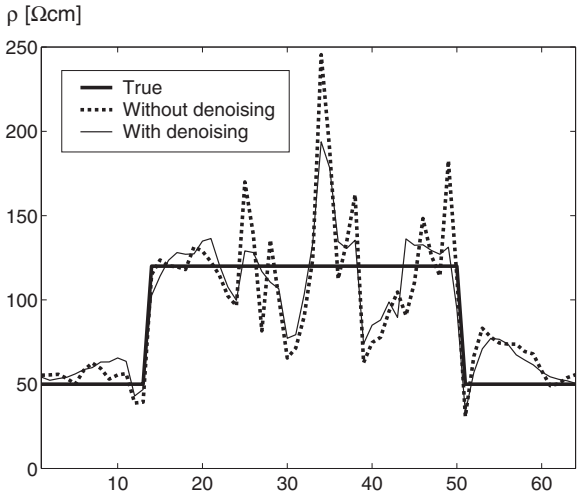

Figure 9. Horizontal profiles around the centre of three resistivity images in figure 8.

Figure 7(b) is the difference between these two profiles. To estimate the noise standard deviations in $|\mathbf{J}|$, we computed the difference between two $|\mathbf{J}|$ images in figures 6(b) and (c). The standard deviations in the difference image were 75 and 265 μA cm^{-2} in the solution and sausage, respectively.

Figure 8(a) shows the true resistivity image of the phantom. Here, we assumed that the resistivity is homogeneous within the solution and sausage. Using the J-substitution algorithm (Kwon *et al* 2002), we reconstructed the resistivity images in figure 8(b) without denoising and (c) with denoising. During the image reconstructions, we used two current density images due to the corresponding two injection currents I_1 and I_2. Figure 9 shows horizontal profiles around the centre of three resistivity images in figure 8. For the resistivity image in figure 8(b) without denoising, the reconstructed average resistivity values were 60.8 and 115.4 Ω cm in the solution and sausage, respectively, compared to the true values of 50.5 and 123.7 Ω cm. For the image in figure 8(c) with denoising, the average values were 60.9 and 117.7 Ω cm in the solution and sausage, respectively. We define the relative L^2-error of the resistivity image as

$$\epsilon_\rho = \frac{\|\rho^* - \rho\|_2}{\|\rho^*\|_2} \times 100\ (\%)$$

where ρ^* and ρ are the true and reconstructed resistivity images, respectively. The computed relative L^2-errors were 32.3 and 25.5% for the images in figures 8(b) and (c), respectively.

4. Discussion

Unlike a saline phantom containing insulating objects, the resistivity values of the phantom used in this paper are within the range of physiologically observed ones. Therefore, the magnitude of current density $|\mathbf{J}|$ is always greater than zero at all pixels. This is one of the reasons why we could get a better image compared with the resistivity image presented by Khang *et al* (2002). Improvements are also due to better phase unwrapping and geometrical error correction methods.

In estimating noise standard deviations of the measured magnetic flux density and current density, we used the differences between images with and without denoising. Since the denoising algorithm used in this paper does not completely remove the noise in measured magnetic flux densities, the estimated noise standard deviations must have been underestimated. Furthermore, in addition to the noise predicted by (5) and (6), the images of $|\mathbf{J}|$ shown in figures 6(b) and (c) contain other kinds of errors. These include the misalignment of pixels among different slices of magnetic flux density images and errors in numerical differentiations with the finite sizes of Δx, Δy and Δz. As described by Scott *et al* (1992), the misalignment of pixels should have produced much larger amount of errors compared to the expected noise standard deviations in (5) and (6). We speculate that the white rings around the edge of the sausage in figures 6(b) and (c) are mainly due to the misalignment of pixels. Since errors in $|\mathbf{J}|$ are directly transferred to errors in the reconstructed resistivity image using the J-substitution algorithm, we should devise a better way of accurately aligning pixels from different slices.

Currently, we use copper electrodes and these produce artefacts near electrodes. We tried electrodes made of silicone containing silver powder and got unsatisfactory results. Carbon electrodes and lead wires used in EEG measurements during MR imaging should be considered in future studies. In using the J-substitution algorithm, we need at least one boundary voltage datum to appropriately scale the reconstructed resistivity image. This boundary voltage measurement must be made carefully using the four-electrode method. Our future studies should also include better denoising techniques, three-dimensional volume imaging, three-dimensional image reconstruction, image reconstruction within a region of interest, utilization of more electrodes and boundary voltage data, incorporation of *a priori* structural information from MR magnitude images and others.

Most importantly, there are two major technical problems in MREIT. One is the subject rotation procedure to acquire all three components of the induced magnetic flux density. Even though we can reduce the rotation angle at the expense of a reduced SNR in measured magnetic flux density images, any subject rotation in current clinical MR imaging environments seems to be very difficult. The other is the low SNR in MR phase images which makes it difficult to reduce the amount of injection current. To solve the first problem, we should develop a new image reconstruction algorithm utilizing only one component of the induced magnetic flux density such as B_z. For the SNR problem, we should use an MRI scanner with higher SNR and increase the number of averagings and voxel size. Increasing the voxel size will significantly reduce the amount of noise at the expense of scarifying the spatial resolution. Considering the fact that we must reduce the amount of injection current to at most 1 mA

for the human subject, we plan to use a three-dimensional volume imaging technique with about $3 \times 3 \times 3$ mm^3 voxels in our future studies.

5. Conclusion

MREIT utilizes internal current density measurements by the MRCDI technique to overcome the inherent ill-posedness of the EIT image reconstruction problem. Using a 0.3 T experimental MREIT system, we reconstructed a 64×64 resistivity image with $0.6 \times 0.6 \times 10$ mm^3 voxels by injecting currents of 28 mA into a saline phantom of $50 \times 50 \times 50$ mm^3 containing a cylindrical sausage object. Even though the error in the reconstructed average resistivity value was small, the relative L^2-error of the reconstructed resistivity image was 25.5%. We speculate that current density and resistivity images with $3 \times 3 \times 3$ mm^3 voxels in a field of view of about 200 mm could be possible using an injection current of about 1 mA. This will require an MRI scanner with higher SNR. Once we get static resistivity images from the MREIT system, these could also be used as initial conditions or *a priori* information in dynamic or difference imaging in EIT for better results.

Acknowledgments

This work was supported by the grant R11-2002-103 from Korea Science and Engineering Foundation.

References

Chan T, Marquina A and Mulet P 2000 High-order total variation-based image restoration *SIAM J. Sci. Comput.* **22** 503–16

Eyuboglu M, Birgul O and Ider Y Z 2001 A dual modality system for high resolution-true conductivity imaging *Proc. 11th Int. Conf. on Electrical Bioimpedance (ICEBI)* pp 409–13

Eyuboglu M, Reddy R and Leigh J S 1998 Imaging electrical current density using nuclear magnetic resonance *Elektrik* **6** 201–14

Gamba H R, Bayford D and Holder D 1999 Measurement of electrical current density distribution in a simple head phantom with magnetic resonance imaging *Phys. Med. Biol.* **44** 281–91

Gamba H R and Delpy D T 1998 Measurement of electrical current density distribution within the tissues of the head by magnetic resonance imaging *Med. Biol. Eng. Comput.* **36** 165–70

Ghiglia D C and Pritt M D 1998 *Two-Dimensional Phase Unwrapping: Theory, Algorithms and Software* (New York: Wiley Interscience)

Ider Y Z and Birgul O 1998 Use of the magnetic field generated by the internal distribution of injected currents for electrical impedance tomography (MR-EIT) *Elektrik* **6** 215–25

Khang H S, Lee B I, Oh S H, Woo E J, Lee S Y, Cho M H, Kwon O, Yoon J R and Seo J K 2002 *J*-substitution algorithm in magnetic resonance electrical impedance tomography (MREIT): phantom experiments for static resistivity images *IEEE Trans. Med. Imag.* **21** 695–702

Kim S W, Kwon O, Seo J K and Yoon J R 2002 On a nonlinear partial differential equation arising in magnetic resonance electrical impedance tomography *SIAM J. Math. Anal.* **34** 511–26

Kwon O, Woo E J, Yoon J R and Seo J K 2002 Magnetic resonance electrical impedance tomography (MREIT): simulation study of *J*-substitution algorithm *IEEE Trans. Biomed. Eng.* **49** 160–7

Lee B I, Oh S H, Woo E J, Lee S Y, Cho M H, Kwon O, Yoon J R and Seo J K 2002 Three-dimensional forward problem in magnetic resonance electrical impedance tomography (MREIT) *Proc. 2nd Joint IEEE EMBS/BMES Conf. (Houston, TX)* pp 967–8

Oh S H, Lee B I, Woo E J, Lee S Y, Cho M H, Kwon O, Yoon J R and Seo J K 2002 Magnetic resonance electrical impedance tomography (MREIT): phantom experiments for static resistivity images using *J*-substitution algorithm *Proc. 2nd Joint IEEE EMBS/BMES Conf. (Houston, TX)* pp 917–8

Scott G C, Joy M L G, Armstrong R L and Henkelman R M 1991 Measurement of nonuniform current density by magnetic resonance *IEEE Trans. Med. Imag.* **10** 362–74

Scott G C, Joy M L G, Armstrong R L and Henkelman R M 1992 Sensitivity of magnetic-resonance current density imaging *J. Mag. Res.* **97** 235–54

Woo E J, Lee S Y and Mun C W 1994 Impedance tomography using internal current density distribution measured by nuclear magnetic resonance *SPIE* **2299** 377–85

Zhang N 1992 Electrical impedance tomography based on current density imaging *MS Thesis* Department of Electrical Engineering, University of Toronto